remote sensing

MDPI

Article

Monitoring Early Growth and Canopy Structural Responses in Young Chinese Fir Plantations Using UAV-LiDAR

Xinyu Liang [1], Hongda Zeng [1,*], Jing M. Chen [1,2], Zhiqun Huang [1] and Bowen Yang [1]

[1] Institute of Geography, Key Laboratory for Humid Subtropical Eco-geographical Processes of the Ministry of Education, Fujian Normal University, Fuzhou 350117, China
[2] Department of Geography and Planning, University of Toronto, 100 St. George Street, Toronto, ON M5S 3G3, Canada
* Correspondence: zeng.hd@fjnu.edu.cn

Highlights

What are the main findings?

- Bi-temporal UAV-LiDAR reliably quantified tree-height increments and extended monitoring to model-based diameter and biomass increments.
- UAV-LiDAR-derived growth metrics captured trends associated with planting density, slope position, and planting-pit size.
- Canopy metrics correlated significantly with early growth, although most showed no significant management-related differences.

What are the implications of the main findings?

- Combining bi-temporal growth and canopy metrics supports evaluation of establishment practices at individual-tree and plot scales.

Abstract

Early plantation development is sensitive to establishment practices, but field surveys provide limited information on fine-scale growth and three-dimensional canopy structure. This study evaluated a bi-temporal unmanned aerial vehicle-based light detection and ranging (UAV-LiDAR) workflow in a young Chinese fir plantation. The workflow was used to estimate growth increments at individual-tree and plot scales and to characterize canopy structure under different establishment conditions. UAV-LiDAR surveys were conducted in February and November 2023, with individual trees matched between surveys. Tree height (TH) change was derived directly from the two LiDAR acquisitions, whereas diameter at ground level (DGL), aboveground biomass (AGB), and their increments were estimated using a TH–DGL model and an allometric equation. Against November field data, the root mean square errors for TH, DGL, and AGB were 0.29 m, 0.65 cm, and 0.13 kg at the individual-tree scale and 0.11 m, 0.35 cm, and 0.45 t·ha^{-1} at the plot scale, respectively. Low planting density was associated with larger individual-tree DGL and AGB, whereas high density had greater plot-level AGB increment (ΔAGB) than low density. Among the canopy metrics, only maximum leaf area density (LAD_{max}) differed significantly among density treatments, with higher values under medium and high densities than under low density. Nevertheless, ΔAGB was significantly positively correlated with leaf area index, canopy cover, LAD_{max}, and foliage peak height (ρ = 0.511–0.808) and significantly negatively correlated with the Weibull shape parameter k, which characterizes the form of the vertical foliage distribution (ρ = −0.515). These relationships show that early biomass accumulation was closely associated with canopy structural metrics.

Academic Editors: Aobo Liu, Xiaoxiao Zhu, Cangjiao Wang and Yating Chen

Received: 14 October 2026
Revised: 25 November 2026
Accepted: 27 November 2026
Published: 29 November 2026

Copyright: © 2026 by the authors. Licensee MDPI, Basel, Switzerland. This article is an open access article distributed under the terms and conditions of the Creative Commons Attribution (CC BY) license.

Exploratory comparisons among six slope-position × planting-pit-size plots showed additional plot-specific variation in growth and canopy structure. Overall, the bi-temporal UAV-LiDAR workflow integrated LiDAR-derived TH changes, model-based DGL and AGB changes, and three-dimensional canopy metrics to characterize early plantation development across scales.

Keywords: UAV-LiDAR; Chinese fir plantations; planting density; canopy structural parameters; growth monitoring

1. Introduction

Forests play a fundamental role in regulating the global carbon cycle, maintaining ecological stability, and providing essential ecosystem services [1,2]. Among forest types, plantations constitute an important component of global forest resources. During establishment, plantations undergo rapid structural reorganization, which shapes their subsequent growth trajectories and biomass accumulation [3,4]. Reliable monitoring of this early stage is therefore important for evaluating plantation establishment and supporting timely silvicultural decisions [5,6]. However, conventional field inventories are labor-intensive and generally focus on tree height and stem diameter, providing limited information on the spatially continuous and three-dimensional development of young plantation canopies.

Chinese fir *(Cunninghamia lanceolata* (Lamb.) Hook.*)* is one of the most widely planted fast-growing timber species in southern China. Young Chinese fir plantations provide a relevant setting for investigating how establishment practices and site conditions influence early tree growth and canopy development. In mountainous plantations, early stand development spans the period from seedling establishment to the onset of competition among trees. During this period, rapid changes in root development, photosynthetic capacity, and stress tolerance make tree growth particularly sensitive to establishment practices [5]. This developmental trajectory is jointly shaped by silvicultural practices, particularly planting density and planting-pit size, and by spatially heterogeneous site conditions associated with slope position. Planting density regulates competition for light, water, and nutrients among trees, thereby directly affecting stand growth and canopy architecture [6,7]. Planting-pit size modifies rooting space and local soil moisture and nutrient conditions, consequently influencing seedling survival and subsequent growth [8]. Slope position reflects hillslope variation in moisture and thermal conditions as well as nutrient distribution, resulting in spatial differentiation in the growth of young plantations [9–11]. The combined effects of these factors are initially reflected in canopy space occupation and structural development, which subsequently influence light interception and water-resource acquisition, and ultimately affect individual-tree growth and biomass accumulation [12–14].

Canopy structure complements tree-size measurements when comparing young plantations across planting densities, planting-pit sizes, and slope positions. It describes how foliage and woody components occupy space and helps characterize the within-stand environment [15–17]. However, many key structural attributes, such as canopy cover, leaf area index, leaf area density (LAD) profiles, and internal canopy heterogeneity, are difficult to measure comprehensively through conventional ground surveys [18,19]. Light detection and ranging (LiDAR) provides three-dimensional point clouds that enable the retrieval of tree dimensions, canopy space occupation, and vertical foliage distribution. Weibull functions have been used to summarize LiDAR-derived vertical foliage profiles [20], while subsequent studies demonstrated the complementary value of vertical profile

metrics for estimating forest structural attributes [21]. The Weibull shape parameter (k) characterizes the form of the vertical foliage distribution, whereas the scale parameter (λ) reflects its vertical distribution scale [20,21]. Because planting density, planting-pit size, and slope position may affect resource competition and availability [6–11], the Weibull parameters may reflect differences in canopy structural development under different establishment conditions. With its flexible deployment and high point density, unmanned aerial vehicle-based LiDAR (UAV-LiDAR) has been used for individual-tree detection and canopy-structure assessment in young or managed plantations [22,23], although many studies have relied on single-survey observations. Previous studies reported individual-tree detection F-scores of approximately 0.93–0.99 in young pine stands [22] and 0.921 in a Chinese fir plantation [24].

Multitemporal point-cloud acquisitions have extended forest remote sensing from static structural assessment to the monitoring of forest growth and biomass change. Bi-temporal UAV photogrammetric point clouds have been used to quantify structural development in planted forests [25], whereas repeated airborne LiDAR has supported the estimation of periodic height increments and changes in forest carbon density [26,27]. However, Riofrío et al. [26] reported plot-level height root mean square errors (RMSEs) of 2.63 and 2.77 m for the 2012 and 2018 acquisitions, respectively, while the RMSE of height increment over the 2012–2018 interval was 2.36 m (coefficient of determination, $R^2 = 0.12$). At the UAV scale, Xiong et al. [28] estimated annual biomass growth in a 17-year-old Chinese fir plantation, reporting RMSEs of 0.13 m for tree height and 1.96 cm for diameter at breast height (DBH) estimated from tree height and crown diameter. Their plot-level indirect model based on tree height and crown diameter estimated annual aboveground biomass (AGB) growth with an RMSE of 1.81 $Mg \cdot ha^{-1} \cdot yr^{-1}$ (relative root mean square error, rRMSE = 17.10%). Yin et al. [29] quantified multiyear tree-height growth in mangrove forests, reporting deviations of −9 to +11 cm from field-measured heights, with a deviation of only 1 cm when the same sensor was used across surveys. Despite these advances, short-interval change estimation remains more sensitive than single-date attribute retrieval to point-cloud registration, terrain normalization, segmentation consistency, acquisition configuration, and measurement error [26,30,31]. These challenges are especially relevant to recently established plantations before canopy closure, where trees are small and diameter at ground level (DGL) cannot be directly retrieved from top-down UAV-LiDAR observations. Comparatively few studies have evaluated an integrated bi-temporal UAV-LiDAR workflow that maintains individual-tree correspondence across surveys, extends directly observed height change to model-based DGL and AGB changes, and links tree-level growth estimates with plot-level canopy structural metrics. Further evaluation is therefore needed to determine whether LiDAR-derived LAD profiles and Weibull parameters provide structural information complementary to short-interval tree growth and biomass estimates. Such integration may also offer additional insights into growth differences among plantation management practices and help identify potential canopy structural predictors for future forest growth modeling.

To address these research gaps, we developed and evaluated a bi-temporal UAV-LiDAR workflow for monitoring short-interval growth and characterizing canopy structural variation in a young Chinese fir plantation established in 2022 in a mountainous subtropical region. Specifically, this study aimed to: (1) evaluate individual tree detection and UAV-LiDAR estimates of tree height, diameter at ground level, and aboveground biomass, including their changes between the two surveys; (2) quantify individual-tree growth and plot-level biomass accumulation across planting densities, while exploring growth differences associated with planting-pit size and slope position; and (3) characterize canopy structural variation across planting densities and conduct exploratory

comparisons of canopy structural characteristics associated with planting-pit size and slope position.

2. Materials and Methods

2.1. Study Area

The study was conducted at the Baisha State-owned Forest Farm in Shanghang County, Longyan City, Fujian Province, China (25°08′59″N, 116°36′47″E) (Figure 1). The region has a humid subtropical monsoon climate, with a mean annual temperature of 19.8 °C and a mean annual precipitation of 1637 mm during 2000–2020. Precipitation is mainly concentrated from spring to summer. The coincidence of relatively warm temperatures and abundant precipitation during spring and summer provides favorable conditions for the main growing period of young Chinese fir. From autumn to early spring, rainfall events are generally less frequent and weather conditions are relatively stable, often providing precipitation-free survey windows with low wind speeds and good visibility for UAV-LiDAR data acquisition. The soils are red soils derived from granite, predominantly clay loam, with a depth exceeding 60 cm, which is suitable for Chinese fir growth. The experimental site was established on a harvested 35-year-old Masson pine (*Pinus massoniana*) stand. Harvest residues were retained, and site preparation was carried out using pit-based methods. Planting was completed in late March 2022, covering a total area of 11.6 ha. The plantation was established within the larger field experimental site and research platform named the "Subtropical forest plantation experimental site to increase carbon sequestration". Twenty-one pure Chinese fir plots, each measuring 20 m × 20 m, were selected for the present study. The mean slope was 25°. At the time of the 2023 field survey, the stand was two years old, with a mean diameter at ground level (DGL) of 5.73 cm and a mean tree height (TH) of 2.55 m.

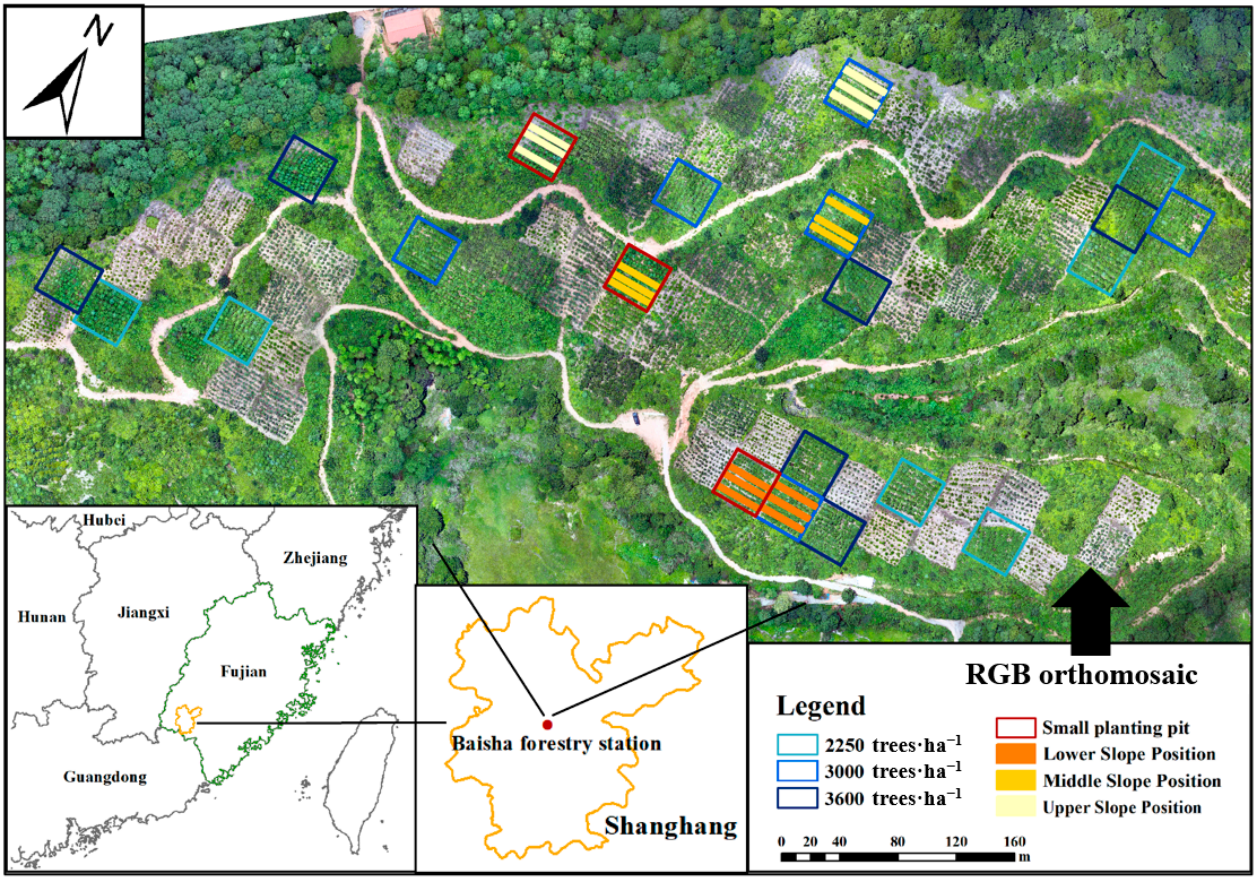


Figure 1. Location map of the study area. The background is an RGB orthomosaic acquired using a DJI Mavic 3 Multispectral UAV in July 2023, with a spatial resolution of approximately 3.35 cm. Light blue, blue, and dark blue outlines indicate planting densities of 2250, 3000, and 3600 trees·ha^{-1}, respectively, with six plots per density. Orange, yellow, and light yellow fills represent lower, middle, and upper slope positions, respectively. Red outlines indicate small-pit plots, while all remaining plots used large planting pits. Three medium-density, large-pit plots were shared between the two experimental components, resulting in 21 unique plots.

2.2. UAV-LiDAR Data

UAV-LiDAR data were acquired on 2 February and 23 November 2023 using a D2000 multirotor UAV (Feima Robotics, Shenzhen, China) equipped with a Hesai XT32 LiDAR sensor. The 32-channel mechanical scanner operated at 20 Hz in triple-return mode, with a vertical angular resolution of 1.3°. Both surveys were conducted using the same flight lines and acquisition parameters, including a flight altitude of 100 m above ground level, a cross-grid flight pattern, a scan zenith range of ±35°, and 60% flight-line overlap. Coordinates were recorded in WGS 84/UTM Zone 50N, and flight trajectories were independently post-processed using the Qianxun post-processing kinematic (PPK) service. No additional ground-control-point-based co-registration was performed between the two point clouds after PPK processing. The average point-cloud densities for the February and November datasets were approximately 195 and 227 points·m^{-2}, respectively (Figure 2).

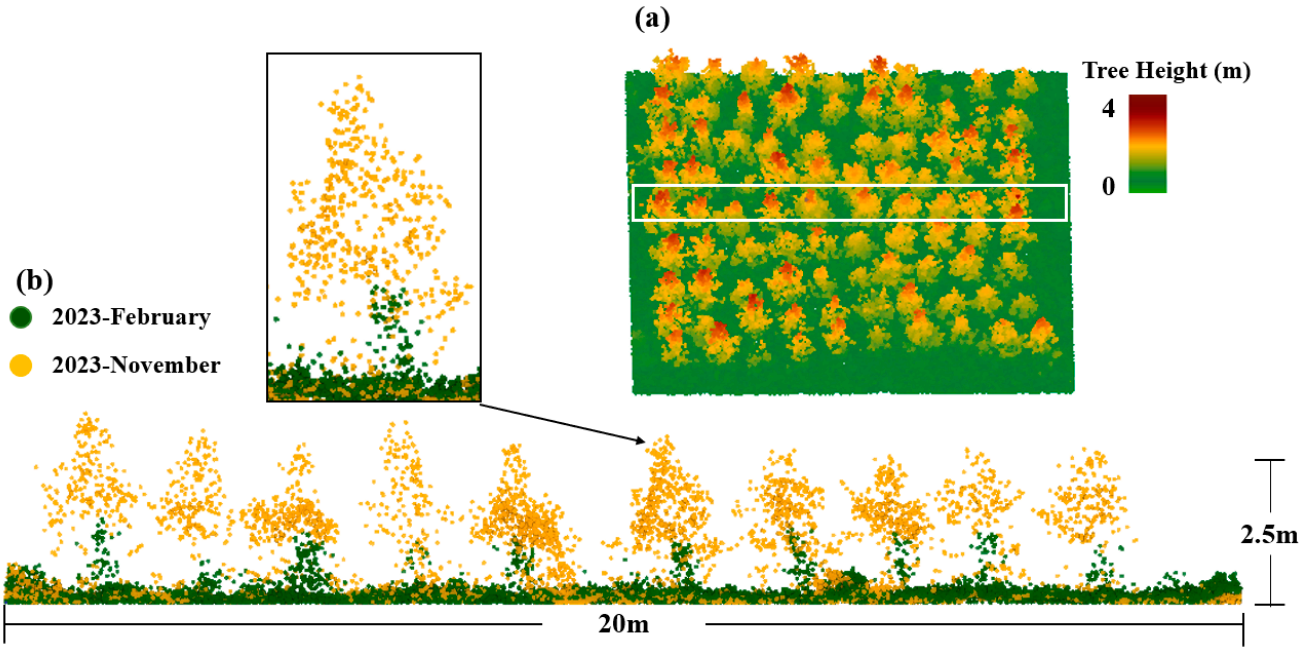


Figure 2. UAV-LiDAR point-cloud data acquired in February and November 2023: (**a**) Three-dimensional point cloud of the study area; (**b**) Bi-temporal point cloud profiles along a 20 m transect (0.5 m wide).

The point clouds were first denoised using a three-standard-deviation threshold based on point distances from locally fitted planes, followed by visual inspection in profile views and manual removal of any remaining noise points. Ground points were then classified using an improved progressive triangulated irregular network (TIN) densification algorithm. To evaluate the vertical accuracy of the two datasets, separate digital elevation models (DEMs) were generated from the classified ground points of both datasets using TIN interpolation and independently validated against the same 108 real-time kinematic (RTK)-measured ground reference points. Both DEMs showed small vertical deviations

from the RTK reference elevations. Given the relatively limited canopy obstruction in February, the February DEM was selected as the common terrain reference for height normalization of both point clouds. Separate digital surface models (DSMs) were generated for the two dates using kriging interpolation. The corresponding canopy height models (CHMs) were then generated at a spatial resolution of 0.1 m by subtracting the common DEM from the respective DSMs. Both CHMs were smoothed using a Gaussian filter with identical parameters (σ = 1 and a window parameter of 5 pixels) to reduce local height irregularities and ensure consistent preprocessing between the two acquisition dates.

Initial treetop seed points were extracted from the smoothed February CHM using a watershed-based segmentation algorithm [32] and manually adjusted against UAV orthomosaics. The revised seed points were first used to guide individual-tree segmentation in the height-normalized February point cloud and then applied to the height-normalized November point cloud for segmentation. Individual-tree detection accuracy was evaluated using the November segmentation results before any subsequent manual correction of the segmentation results. Following the accuracy assessment, the segmentation results from both dates were visually inspected against the corresponding UAV orthomosaics and manually corrected where necessary. The corrected individual-tree datasets were then matched between dates in ArcGIS 10.4 based on tree coordinates. Tree height (TH) was extracted from the height-normalized individual-tree point clouds, while crown diameter (CD) was calculated from the horizontal crown projection area using an equivalent-area circle method. All point-cloud preprocessing and individual-tree segmentation were performed in LiDAR360 6.0 (Beijing GreenValley Technology Co., Ltd., Beijing, China).

2.3. Plot Design and Data Survey

The study comprised 21 unique plots (20 m × 20 m) across two experimental components: a planting density experiment and a complementary comparison of slope position and planting-pit size (Figure 1). For the planting density experiment, 18 plots were arranged into three blocks according to the canopy height of the previous Masson pine stand and mean plot elevation, with six plots per block. Three planting densities were evaluated: low (2250 trees·ha^{-1}), medium (3000 trees·ha^{-1}), and high (3600 trees·ha^{-1}). Each density treatment was represented by two plots within each block, resulting in six plots per treatment across the three blocks. All 18 plots were established using large planting pits measuring 60 cm × 40 cm × 40 cm.

A complementary comparison was conducted to characterize growth and canopy structural patterns associated with slope position and planting-pit size. Six plots with a uniform planting density of 3000 trees·ha^{-1} were selected across upper, middle, and lower slope positions. Slope positions were determined based on the relative locations of the plots along the hillslope, considering plot elevation, local topographic conditions, and contour information (Figure 3). The corresponding elevation ranges were 570–585 m, 550–560 m, and 540–545 m, respectively. At each slope position, one plot was established using large planting pits (60 cm × 40 cm × 40 cm), while the other used small planting pits (30 cm × 30 cm × 15 cm). The three large-pit plots were shared with the planting density experiment and retained their original block assignments, while the three additional small-pit plots were excluded from the density analyses. Within each of the six plots, three 20 m × 3 m belt transects were established approximately along the contour lines. Canopy structural metrics were calculated for each belt transect and then summarized across the three transects at the plot level.

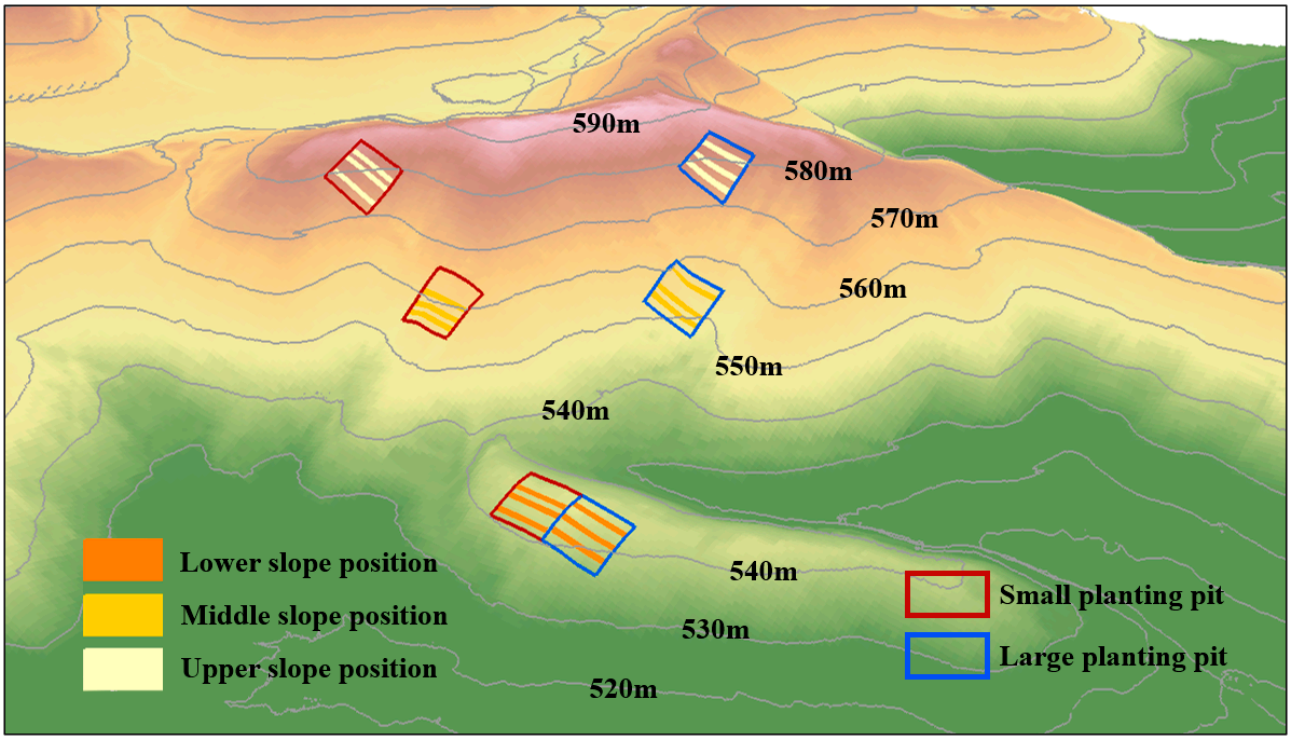


Figure 3. Topography of the study area and distribution of planting-pit treatments across slope positions. The digital elevation model (DEM) was generated from ground-classified returns of UAV-LiDAR data acquired on 2 February 2023 at a spatial resolution of 0.1 m. The coordinate reference system is WGS 84/UTM Zone 50N, and the contour interval is 10 m.

In November 2023, a complete field inventory was conducted for all surviving trees. TH was measured using a 5 m aluminum leveling staff, and DGL was recorded using a vernier caliper with an accuracy of 0.01 mm. Field-measured TH was recorded to the nearest 0.1 m, and LiDAR-derived TH was rounded to the same precision for consistency in accuracy assessment. Aboveground biomass (AGB) was calculated for each tree from the measured TH and DGL using a published allometric equation for Chinese fir (Table 1) [33]. Plot-level AGB was obtained by aggregating the individual tree estimates and scaling them to a per-hectare basis. These field-derived values were used to evaluate the accuracy of UAV-LiDAR estimates.

In addition, plot corners and 200 reference trees were precisely georeferenced using a Galaxy G6 real-time kinematic Global Navigation Satellite System receiver (South Surveying & Mapping Technology Co., Ltd., Guangdong, China). The positions of the reference trees were further refined using orthomosaics acquired with a DJI Mavic 3 Multispectral UAV. The resulting coordinates were used to match field trees with individual trees delineated from the UAV-LiDAR data.

Table 1. Allometric biomass equation for estimating aboveground biomass.

Equation	Accuracy
$y_{leaf} = 32.33994 DGL^{1.610275} TH^{0.2229309}$	$R^2 = 0.984$
$y_{branch} = 7.711003 DGL^{2.112457} TH^{0.1948700}$	$R^2 = 0.981$
$y_{trunk} = 11.19123 DGL^{1.527634} TH^{1.315277}$	$R^2 = 0.998$
$y_{bark} = 4.104651 DGL^{1.795868} TH^{0.2790985}$	$R^2 = 0.992$
$y = y_{trunk} + y_{branch} + y_{leaf} + y_{bark}$	

Where y represents individual tree aboveground biomass, DGL represents diameter at ground level, TH represents tree height, and $y_{leaf}, y_{branch}, y_{trunk}, y_{bark}$ refer to the biomass of tree leaves, branches, trunk and bark.

2.4. Estimation of Forest Growth and Canopy Structure Parameters

Variables obtained from UAV-LiDAR were grouped into growth and canopy structural parameters. The growth parameters included TH, DGL, AGB, and their growing-season increments (ΔTH, ΔDGL, and ΔAGB). TH was obtained as the maximum height within each segmented, height-normalized point cloud. Because TH was directly retrieved from the UAV-LiDAR data without model calibration, its accuracy was evaluated against field-measured TH for all 200 reference trees. For DGL estimation, the 200 reference trees were randomly divided into two non-overlapping datasets of equal size. A calibration dataset comprising 100 trees was used to fit six candidate models using TH, CD, or their combination as predictors (Table 2). The remaining 100 trees were withheld from model fitting and used exclusively for the independent validation of model-estimated DGL and the subsequently derived AGB.

Table 2. Candidate regression models and their theoretical expressions for estimating diameter at ground level.

Model Form	Theoretical Expression
Power	$DGL = ax^b$
Multiple linear	$DGL = a + b\mathrm{TH} + c\mathrm{CD}$
Multiplicative power	$DGL = a\mathrm{TH}^b\mathrm{CD}^c$
Additive power	$DGL = a\mathrm{TH}^b + c\mathrm{CD}$
Exponential	$DGL = ae^{-b\mathrm{TH}+c\mathrm{CD}}$

Note: DGL represents diameter at ground level (cm), TH represents tree height (m), and CD represents crown diameter (m). In the power models, x denotes either TH or CD. The coefficients *a*, *b*, and *c* are model parameters to be estimated.

Following previous studies that estimated less accessible tree attributes from remotely retrieved structural variables [34–36], model selection was based on statistical significance, goodness of fit, and residual diagnostics. The overall statistical significance of each candidate model was evaluated using an F-test, while the coefficient of determination (R^2) was used to assess model goodness of fit. Residual distributions were also examined to evaluate model adequacy. The final model was selected by considering these criteria together with model parsimony and was subsequently applied to the February and November point clouds. This application assumed that the relationship between the predictor variables and DGL remained stable over the observation interval. At each acquisition date, LiDAR-derived TH and model-estimated DGL were jointly entered into the allometric equation for three-year-old Chinese fir (Table 1) to calculate individual-tree AGB. Consequently, DGL and AGB at both dates, as well as their corresponding changes (ΔDGL and ΔAGB), were treated as model-based estimates. Model fitting and numerical calculations were performed in Python 3.12 using SciPy v1.13.1 [37]. The growing-season increments were calculated by subtracting the February 2023 estimates from the corresponding November estimates. Although the two surveys were separated by approximately 9.7 months, local observations of height growth phenology and regional MODIS phenology indicate that this interval encompasses the principal growing season of young Chinese fir in subtropical Fujian [38,39]. The observed differences were therefore interpreted as phenology-supported estimates of growing-season growth, without linear temporal scaling. ΔTH, ΔDGL, and individual-tree ΔAGB were expressed in m, cm, and kg, respectively, while plot-level ΔAGB was expressed in $t \cdot ha^{-1}$.

Canopy structural parameters were calculated exclusively from the UAV-LiDAR data acquired in November 2023. Canopy cover (CC), leaf area density (LAD), and leaf area index (LAI) were derived from the height-normalized point clouds as described in Table 3. To further characterize the vertical distribution of canopy foliage, a two-

parameter Weibull function was fitted to the LAD profiles. The shape (k) and scale (λ) parameters were estimated using nonlinear least squares, and model goodness of fit was evaluated using the coefficient of determination (R^2). LAD_{max} was defined as the maximum value of the original LAD vertical profile, whereas foliage peak height was determined from the position of the maximum value of the fitted Weibull curve and converted to the corresponding physical height. The overall workflow is shown in Figure 4.

Table 3. Definitions of canopy structural metrics derived from UAV-LiDAR point clouds.

Variables	Formula	Description
CC	$CC = \frac{\sum_{z=t_{canopy}}^{z=\max(z)} C_{first}}{\sum_{z=0}^{z=\max(z)} C_{first}}$ where t_{canopy} is the height threshold (set to 0.5 m) used to exclude understory vegetation, and C_{first} represents the number of first returns within the area.	Canopy cover represents the horizontal density of the canopy, reflecting the degree of canopy closure, light interception capacity, and space occupancy.
LAD	$P_i = 1 - \frac{n_i}{N_i}$ $LAD_i = -\frac{\cos(\theta_i) ln(P_i)}{G \cdot \Delta z}$ where n_i is the number of points in layer i, N_i is the cumulative number of returns from the ground up to layer i, and θ_i is the mean scan angle in layer i. LAD values below 0.5 m were set to zero to minimize near-ground noise.	Leaf area density ($m^2 \cdot m^{-3}$) was estimated for each height layer from point-count-based gap fractions using the Beer–Lambert formulation, with a vertical layer thickness (Δz) of 0.3 m and an assumed extinction coefficient (G) of 0.5. LAD values below 0.5 m were set to zero to minimize the influence of near-ground vegetation and noise.
LAI	$LAI = \sum LAD_i \ \Delta z$ where LAD_i is the leaf area density in layer i ($m^2 \cdot m^{-3}$), and Δz is the vertical layer thickness (set to 0.3 m).	Leaf area index ($m^2 \cdot m^{-2}$) derived by vertically integrating the LAD profile. It represents the total one-sided leaf area per unit ground surface area.
k and λ parameter	$f(x) = \frac{k}{\lambda}(\frac{x}{\lambda})^{k-1} exp\left(-\left(\frac{x}{\lambda}\right)^k\right)$ $x \geq 0; k, \lambda \geq 0$ where the shape parameter k controls the form of the distribution curve, and the scale parameter λ is related to canopy thickness and the mean height of foliage distribution.	The LAD vertical profile was fitted to a Weibull distribution using non-linear least squares with the Levenberg–Marquardt algorithm.

2.5. Accuracy Assessment and Statistical Analyses

The accuracy of individual tree segmentation was evaluated using recall (R), precision (P), and F-score (F) [40,41]. Lower recall indicates more missed trees, a phenomenon known as under-segmentation in the CHM, while lower precision indicates more falsely detected trees, called over-segmentation. The F-score provides an overall measure that combines omission and commission errors [42]. The agreement between LiDAR-derived estimates and field measurements was further assessed using the coefficient of determination (R^2), root mean square error (RMSE), and relative RMSE (rRMSE).

$$R^2 = 1 - \frac{\sum_{i=1}^{n}(P_i - \hat{P}_i)^2}{\sum_{i=1}^{n}(P_i - \bar{P}_i)^2} \quad (1)$$

$$RMSE = \sqrt{\frac{\sum_{i=1}^{n}(P_i - Q_i)^2}{n}} \quad (2)$$

$$rRMSE = \frac{RMSE}{\bar{Q}} \quad (3)$$

Statistical analyses were performed using IBM SPSS Statistics 26.0 (IBM Corp., Armonk, NY, USA), with significance set at $p < 0.05$. For density analyses, the plot was the experimental unit. Tree height, diameter at ground level, individual-tree biomass, and their growing-season increments were averaged within each plot, whereas stand biomass and its increment were summed by plot and expressed per hectare. Density effects were tested using linear mixed-effects models, with density as a fixed effect and block as a random effect. Following a significant overall density effect, estimated marginal means were compared using Fisher's least significant difference (LSD) test. Spearman's rank correlations between November canopy structural metrics and plot-level growing-season ΔAGB were calculated using Python (n = 18 plots). Because each slope position and planting-pit-size combination was represented by a single plot, these plots were compared descriptively, with trees and belt transects used only to characterize within-plot variation. Comparisons between large- and small-pit plots at each slope position were interpreted as exploratory. Figures were prepared using Origin 9.0 (OriginLab Corp., Northampton, MA, USA).

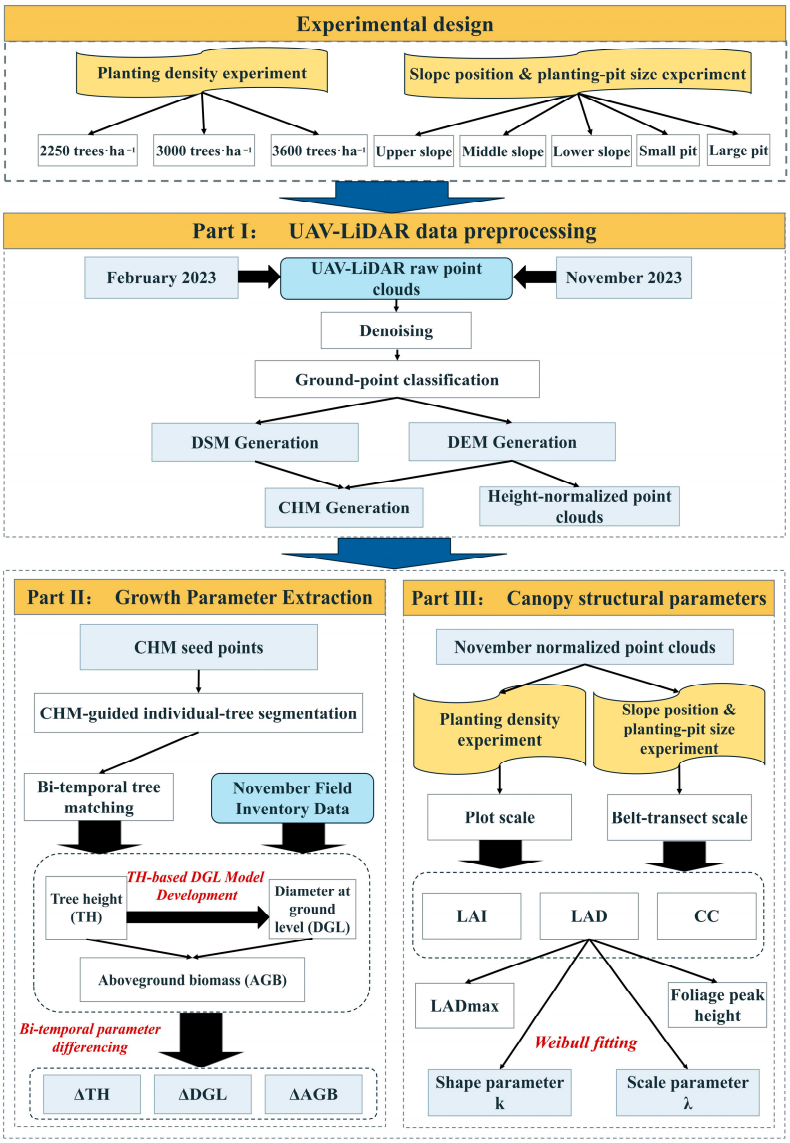


Figure 4. Experimental design and technical workflow of this study.

3. Results

3.1. Individual Tree Recognition and Growth Parameter Monitoring

Accurate individual tree segmentation is essential for reliable AGB estimation. In this study, UAV-LiDAR achieved high segmentation accuracy in the young Chinese fir plantation (Figure 5a), thereby supporting subsequent analyses of growth dynamics and stand structure. A total of 2550 trees were measured in the field, of which 2498 were correctly detected by LiDAR. The remaining 52 trees were missed, and 64 false detections occurred due to over-segmentation. Overall segmentation accuracy was high, with a mean F-score of 0.977, and recall and precision of 0.975 and 0.976, respectively; the minimum values for all three metrics exceeded 0.95 (Figure 5b). At the plot level, segmentation F-scores showed a slight numerical decline with increasing planting density (Figure 5a).

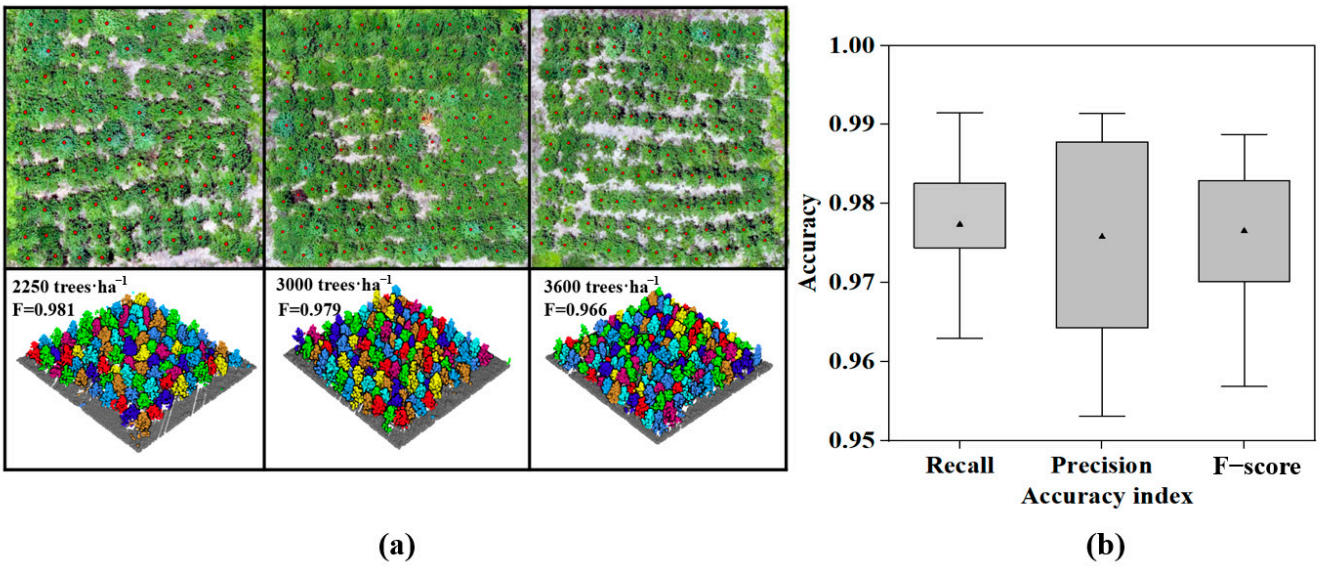


Figure 5. Individual tree segmentation accuracy. (**a**) Seed-point distribution and segmentation results under three planting densities; (**b**) Boxplots of segmentation accuracy metrics.

All six candidate DGL models showed statistically significant relationships according to the overall F-tests (all $p < 0.01$; Table 4). The residuals of all six models showed no significant departures from normality. Among these models, the TH-based power function (M1) provided the best fit, with the highest R^2 value of 0.723 (Table 4; Figure 6b). Considering its goodness of fit, residual characteristics, and parsimonious structure, M1 was selected to estimate DGL at both survey dates. The February TH values fell entirely within the range represented by the November training dataset (Figure 6a), indicating that application of the model to the February data did not require numerical extrapolation beyond the calibrated predictor range. Individual-tree AGB at each survey date was subsequently calculated from LiDAR-derived TH and model-estimated DGL using the published allometric equation for Chinese fir (Table 1).

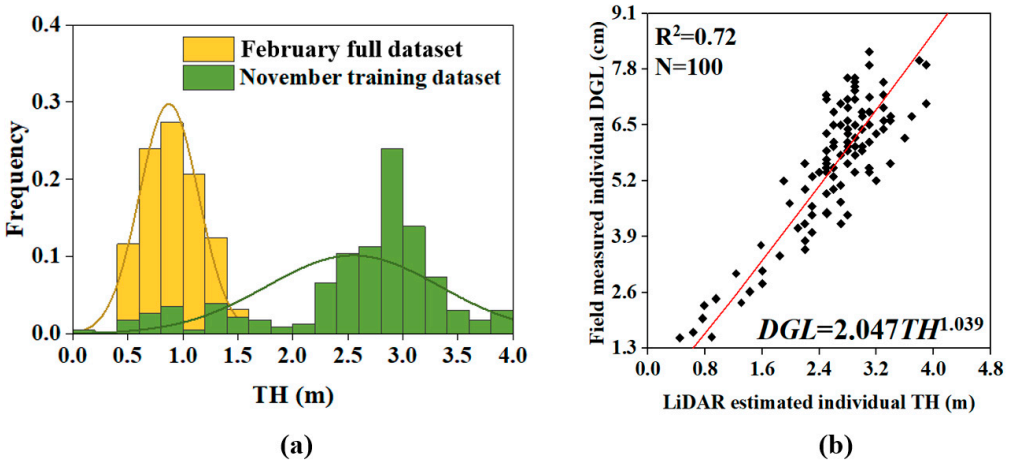


Figure 6. Calibration data and fitted relationship for the selected TH-based model for estimating diameter at ground level (DGL). (**a**) Distributions of LiDAR-derived TH for all trees detected in February and for the November training dataset; (**b**) fitted relationship between UAV-LiDAR-derived TH and field-measured DGL for the 100 trees used exclusively for model calibration. The independent validation dataset comprised the remaining 100 reference trees and was not used for model fitting.

Table 4. Theoretical expressions and fitting statistics of candidate models for estimating diameter at ground level in young Chinese fir plantations.

Model	Predictors	Model Form	Fitted Equation	R^2
M1	TH	Power	$DGL = 2.047TH^{1.039}$	0.723
M2	CD	Power	$DGL = 4.250CD^{0.662}$	0.491
M3	TH, CD	Multiple linear	$DGL = 0.414 + 1.474TH + 0.874CD$	0.561
M4	TH, CD	Multiplicative Power	$DGL = 2.758TH^{0.656}CD^{0.220}$	0.561
M5	TH, CD	Additive power	$DGL = 1.939TH^{0.845} + 0.849CD$	0.566
M6	TH, CD	Exponential	$DGL = 2.355e^{-0.238TH+0.157CD}$	0.516

Note: DGL is diameter at ground level, TH is tree height, and CD is crown diameter. R^2 denotes the coefficient of determination.

LiDAR-derived estimates agreed well with field measurements (Figure 7). At the individual-tree level, TH was estimated with the highest accuracy (R^2 = 0.75, RMSE = 0.29 m, rRMSE = 10.91%), followed by DGL (R^2 = 0.59, RMSE = 0.65 cm, rRMSE = 11.03%) and AGB (R^2 = 0.71, RMSE = 0.13 kg, rRMSE = 13.26%). Slight overestimation was observed for TH and DGL at lower values. For the eight independent validation trees with TH between 0.5 and 1.5 m, the rRMSE values were 8.37%, 10.41%, and 10.36% for TH, DGL, and AGB, respectively; the DGL estimates had an RMSE of 0.19 cm and a bias of 0.06 cm. These relative errors were lower than those obtained for the complete validation datasets. At the plot level, the agreement between LiDAR-derived estimates and field measurements was generally stronger, with R^2 values of 0.82, 0.64, and 0.72 for TH, DGL, and AGB, respectively, and corresponding RMSE values of 0.11 m, 0.35 cm, and 0.45 $t \cdot ha^{-1}$. The lower relative errors at the plot level suggest that spatial aggregation produced more stable estimates.

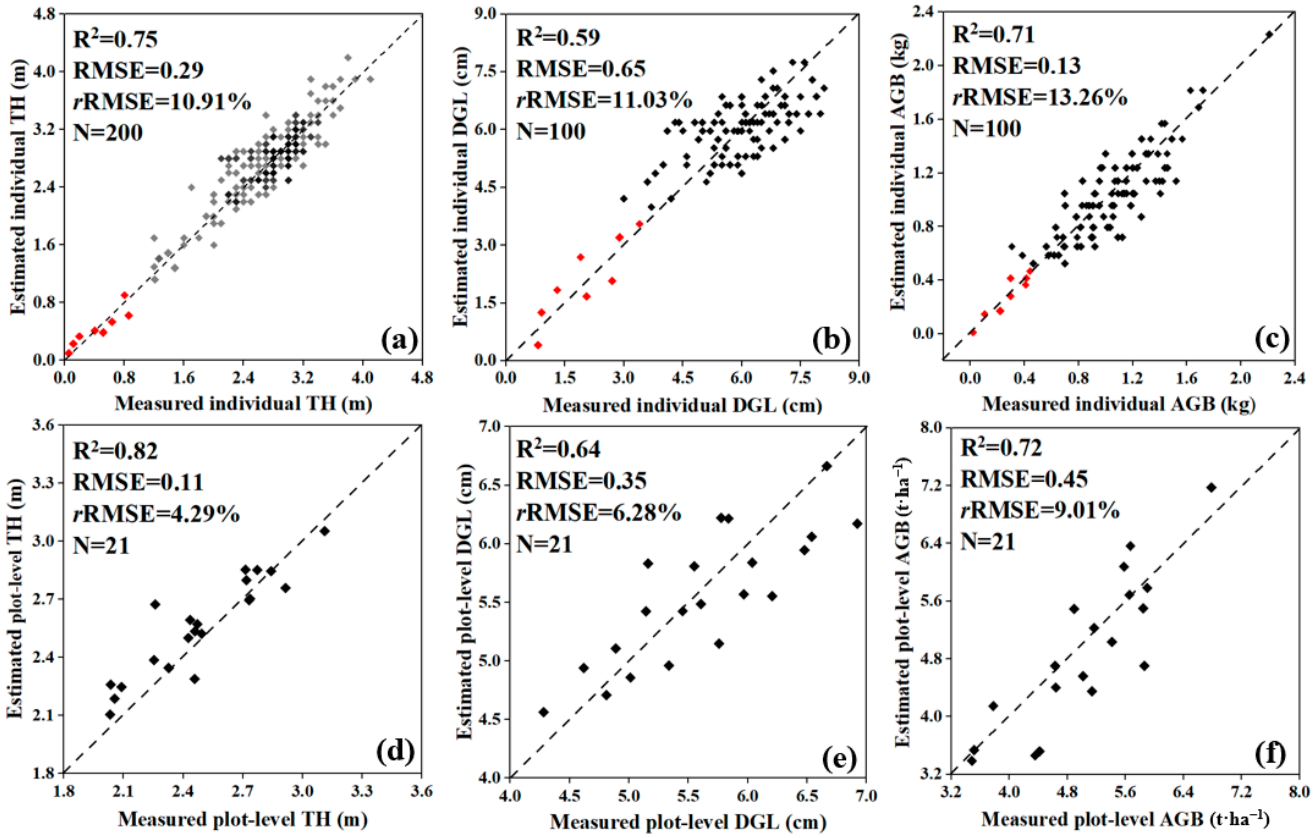


Figure 7. Relationships between LiDAR-derived and field-measured TH, DGL, and AGB at the individual-tree and plot levels. (**a**–**c**) Individual-tree level; (**d**–**f**) plot level. The dashed lines represent the 1:1 relationship. In panel (**a**), semi-transparent gray points are used to visualize overlapping observations, with darker shades indicating greater point overlap. Red points in panels (**a**–**c**) represent the eight trees with field-measured TH between 0.5 and 1.5 m in the November independent validation dataset. The statistics displayed in each panel include R^2, RMSE, rRMSE, and sample size (N). At the individual-tree level, TH accuracy was evaluated using all 200 reference trees because TH was directly retrieved from the UAV-LiDAR data without model calibration (**a**), whereas DGL and AGB accuracy were evaluated using an independent validation dataset of 100 trees withheld from model fitting (**b**,**c**). At the plot level, N = 21 represents the 21 unique plots included in the study (**d**–**f**).

3.2. Response of Growth Parameters to Establishment Treatments

Planting density significantly affected growth characteristics of the young Chinese fir plantation (Figure 8). At the individual tree level, TH did not differ significantly among density treatments ($p > 0.05$). In contrast, DGL was significantly larger in low-density stands than in medium- and high-density stands ($p < 0.05$). Individual tree AGB showed a similar pattern, with higher values under low density. However, at the plot level, AGB accumulation displayed the opposite trend. High-density stands showed a significantly higher ΔAGB (5.19 t·ha^{-1}) than that of low-density stands (3.95 t·ha^{-1}; $p < 0.05$).

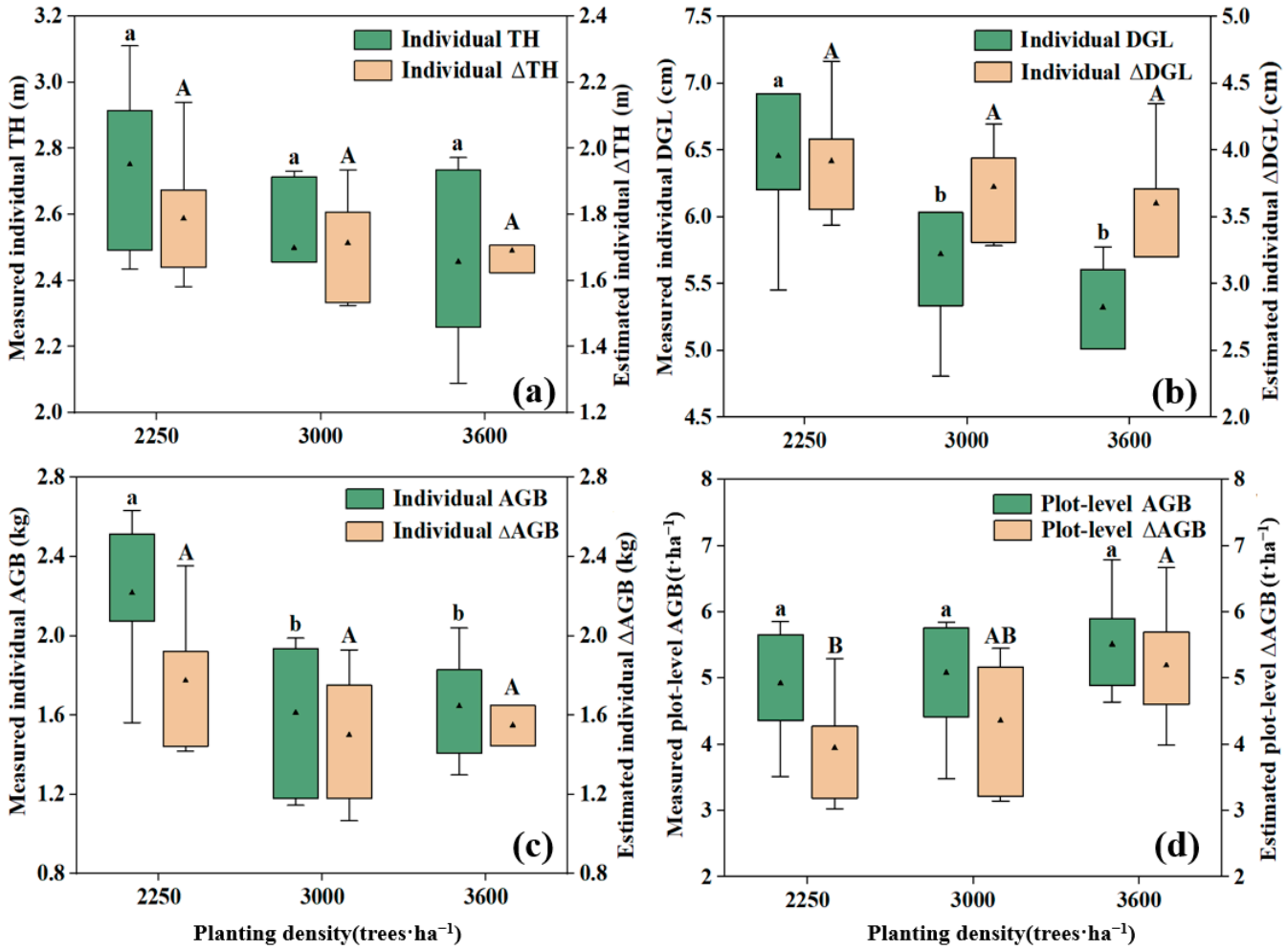


Figure 8. Effects of planting density on tree growth and biomass accumulation in young Chinese fir plantations. (**a**) Mean TH and ΔTH; (**b**) Mean DGL and ΔDGL; (**c**) Mean individual tree AGB and ΔAGB; (**d**) Plot-level AGB and ΔAGB. Different lowercase letters indicate significant differences among treatments for mean values ($p < 0.05$), whereas uppercase letters indicate significant differences for increments ($p < 0.05$). Each density treatment included six plots ($n = 6$).

Descriptive comparisons revealed distinct growth patterns among the six plots representing different combinations of slope position and planting-pit size (Table 5). Under both pit-size treatments, mean individual-tree TH, DGL, AGB, and ΔAGB generally increased from the upper to the lower slope position. In contrast, the magnitude of the large- versus small-pit contrast varied among slope positions, with the largest differences observed at the upper slope. There, TH, DGL, AGB, ΔTH, and ΔAGB were 21.30%, 22.19%, 51.47%, 30.84%, and 56.80% higher, respectively, in the large-pit plot. The corresponding differences were smaller at the middle slope (6.71–14.53%) and intermediate at the lower slope (9.30–26.60%). Notably, the contrasts between large- and small-pit plots were generally greater for AGB and ΔAGB than for TH and DGL, particularly at the upper slope.

Table 5. Descriptive comparison of individual-tree growth variables between the large- and small-pit plots at three slope positions.

Slope Position	Planting Pit Size	TH (m)	DGL (cm)	AGB (kg)	ΔTH (m)	ΔAGB (kg)
Upper	Large	2.11 ± 0.30	4.46 ± 0.65	1.03 ± 0.31	1.40 ± 0.26	0.94 ± 0.29
	Small	1.74 ± 0.34	3.65 ± 0.74	0.68 ± 0.29	1.07 ± 0.32	0.60 ± 0.28
	Relative Difference	+21.30%	+22.19%	+51.47%	+30.84%	+56.80%
Middle	Large	2.39 ± 0.22	5.06 ± 0.47	1.34 ± 0.28	1.59 ± 0.29	1.21 ± 0.27
	Small	2.23 ± 0.35	4.71 ± 0.77	1.17 ± 0.40	1.49 ± 0.25	1.07 ± 0.36
	Relative Difference	+7.17%	+7.43%	+14.53%	+6.71%	+13.60%
Lower	Large	2.47 ± 0.37	5.25 ± 0.82	1.49 ± 0.51	1.71 ± 0.27	1.38 ± 0.46
	Small	2.26 ± 0.31	4.77 ± 0.68	1.19 ± 0.37	1.50 ± 0.28	1.09 ± 0.35
	Relative Difference	+9.30%	+10.06%	+25.21%	+14.00%	+26.60%

Note: Values are expressed as mean ± within-plot standard deviation across individual trees. "Relative difference" represents the percentage increase in the large-pit plot relative to the small-pit plot at the same slope position.

3.3. Canopy Structural Variation Across Planting Densities and Establishment Conditions

UAV-LiDAR-derived canopy metrics varied among the planting-density treatments (Table 6; Figure 9). As planting density increased from 2250 to 3600 trees·ha^{-1}, LAI increased numerically from 0.94 to 1.16 m^2·m^{-2}, and CC from 0.40 to 0.46, but neither differed significantly among the three densities. Mean LAD_{max} increased from 0.17 ± 0.02 m^2·m^{-3} at 2250 trees·ha^{-1} to 0.21 ± 0.05 m^2·m^{-3} at 3000 trees·ha^{-1} and 0.23 ± 0.04 m^2·m^{-3} at 3600 trees·ha^{-1}. Both the medium- and high-density treatments had significantly higher LAD_{max} than the low-density treatment, while the difference between medium and high density was not significant.

The fitted vertical LAD profiles showed higher peaks at medium and high densities than at low density (Figure 9a). The corresponding segmented individual trees are shown in Figure 9b. Mean foliage peak height ranged from 1.36 to 1.44 m. From low to medium and high density, mean k increased from 2.37 to 2.47 and then decreased to 2.32, whereas mean λ decreased from 4.88 to 4.38 and then increased to 4.56. Foliage peak height, k, and λ did not differ significantly among density treatments.

Across the 18 planting-density plots, ΔAGB showed strong positive correlations with LAI (ρ = 0.808, p < 0.01) and CC (ρ = 0.798, p < 0.01), and moderate positive correlations with LAD_{max} (ρ = 0.600, p < 0.01) and foliage peak height (ρ = 0.511, p < 0.05). A negative correlation was found between ΔAGB and Weibull k (ρ = −0.515, p < 0.05), whereas the correlation with Weibull λ was not significant (ρ = 0.404, p > 0.05) (Figure 10).

Beyond the planting-density comparisons, canopy metrics were calculated for three belt transects within each of the six plots representing the slope-position × planting-pit-size combinations (Table 7; Figure 11). In the large-pit plots, LAI, CC, and LAD_{max} were highest at the middle slope, reaching 1.37 m^2·m^{-2}, 0.52, and 0.26 m^2·m^{-3}, respectively, compared with 0.75 m^2·m^{-2}, 0.32, and 0.18 m^2·m^{-3} at the upper slope and 0.99 m^2·m^{-2}, 0.40, and 0.22 m^2·m^{-3} at the lower slope. The Weibull parameters also varied across slope positions, with k decreasing from 2.56 at the upper slope to 2.42 at the lower slope, whereas λ was highest at the middle slope (4.35). Within each slope position, the large-pit plots consistently showed higher LAI and CC than the corresponding small-pit plots. The largest contrast in LAI occurred at the middle slope, where LAI was 1.37 m^2·m^{-2} in the large-pit plot compared with 0.98 m^2·m^{-2} in the small-pit plot. The Weibull parameters also showed plot-specific differences between pit sizes, but these patterns varied among slope positions. Given the single-plot representation of each slope-position × planting-pit-size

combination, these results are interpreted as descriptive contrasts rather than estimates of treatment effects.

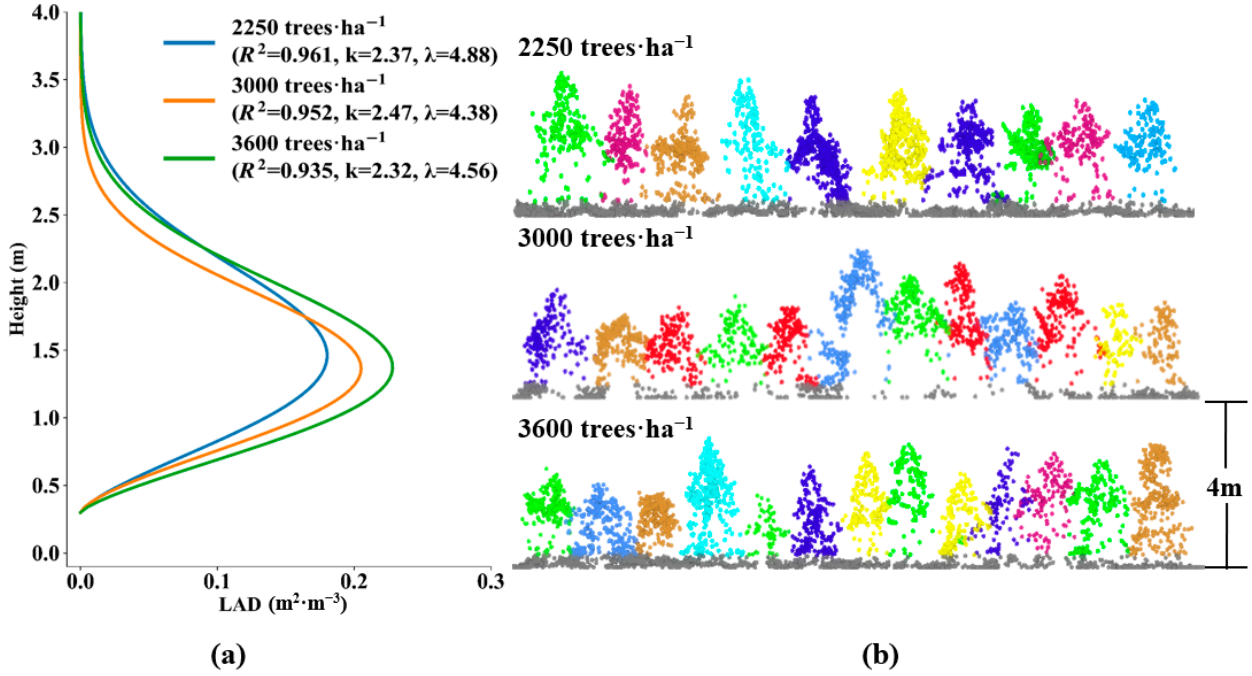


Figure 9. Vertical leaf area density (LAD) profiles and point cloud distributions under different planting-density treatments. (**a**) Vertical LAD profiles fitted using a Weibull function, with R^2 and the estimated parameters shown for each density treatment; (**b**) corresponding point-cloud profiles of representative belt transects, with colors indicating segmented individual trees.

Table 6. Plot-level canopy structural parameters under different planting densities.

Planting Density	LAD_{max} ($m^2 \cdot m^{-3}$)	Foliage Peak Height (m)	LAI ($m^2 \cdot m^{-2}$)	CC	k	λ
Low	0.17 ± 0.02 b	1.44 ± 0.16	0.94 ± 0.17	0.40 ± 0.06	2.37 ± 0.22	4.88 ± 0.37
Medium	0.21 ± 0.05 a	1.36 ± 0.31	0.96 ± 0.32	0.42 ± 0.11	2.47 ± 0.19	4.38 ± 0.46
High	0.23 ± 0.04 a	1.38 ± 0.22	1.16 ± 0.26	0.46 ± 0.07	2.32 ± 0.17	4.56 ± 0.38

Note: Values are presented as mean ± standard deviation (n = 6 plots per density). Different lowercase letters (a and b) within the LAD_{max} column indicate significant differences among planting-density treatments ($p < 0.05$), whereas treatments sharing the same letter are not significantly different. No significant differences were detected for the remaining canopy structural metrics.

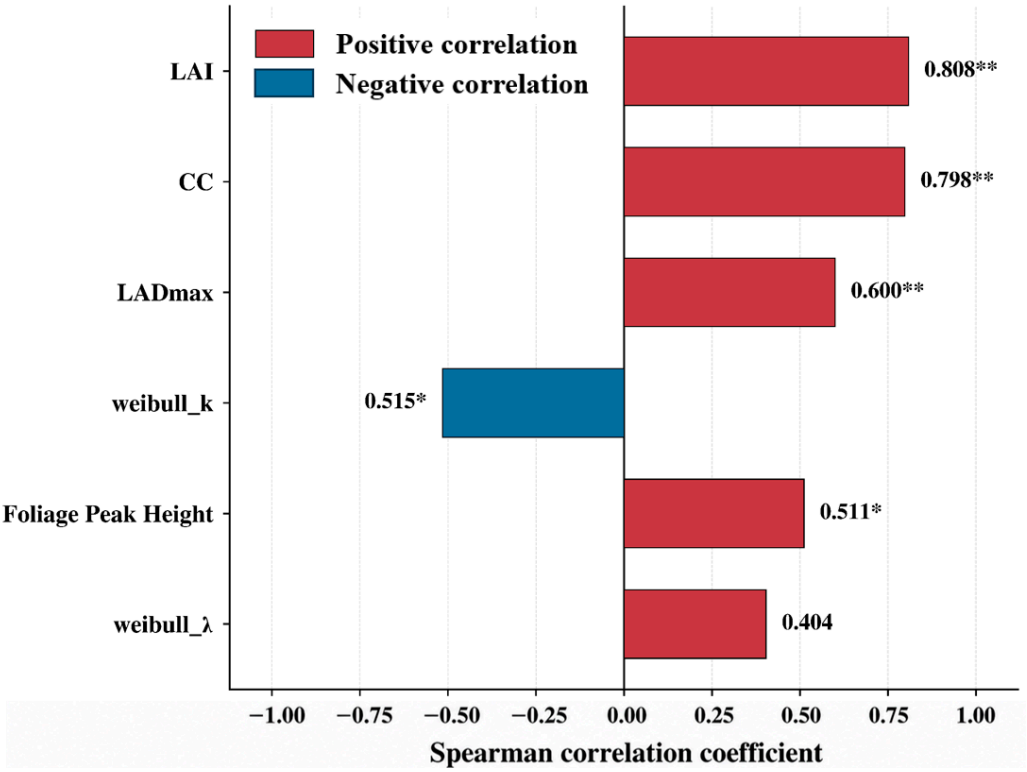


Figure 10. Spearman rank correlations between canopy structural indicators and ΔAGB. Bars represent Spearman's rank correlation coefficients between canopy structural indicators and ΔAGB. Red and blue bars indicate positive and negative correlations, respectively. Numerical labels indicate the absolute magnitudes of the correlation coefficients ($|\rho|$). Asterisks indicate statistical significance (* $p < 0.05$; ** $p < 0.01$; $n = 18$).

Table 7. Descriptive canopy structural metrics for plots differing in slope positions and planting pit sizes.

Plot Combination	LAD_{max} ($m^2 \cdot m^{-3}$)	Foliage Peak Height (m)	LAI ($m^2 \cdot m^{-2}$)	CC	k	λ
Up_B	0.18 ± 0.07	1.28 ± 0.04	0.75 ± 0.24	0.32 ± 0.08	2.56 ± 0.03	4.03 ± 0.05
Up_S	0.15 ± 0.01	1.31 ± 0.03	0.63 ± 0.10	0.28 ±0.05	2.43 ± 0.28	4.29 ± 0.06
Mid_B	0.26 ± 0.05	1.36 ± 0.07	1.37 ± 0.20	0.52 ± 0.04	2.48 ± 0.17	4.35 ± 0.10
Mid_S	0.22 ± 0.03	1.36 ± 0.06	0.98 ± 0.20	0.41 ± 0.07	2.56 ± 0.15	4.23 ± 0.08
Low_B	0.22 ± 0.04	1.32 ± 0.03	0.99 ± 0.07	0.40 ± 0.02	2.42 ± 0.33	4.24 ± 0.03
Low_S	0.15 ± 0.02	1.32 ± 0.15	0.67 ± 0.12	0.29 ± 0.04	2.56 ± 0.13	4.17 ± 0.16

Note: Up, Mid, and Low indicate upper, middle, and lower slope positions, respectively; B and S indicate large and small planting pits, respectively. Values are expressed as the mean ± standard deviation across the three belt transects within each plot. Each combination of slope position and planting pit size was represented by one plot; therefore, the belt transects were not treated as independent treatment replicates, and no inferential tests were conducted. The results should consequently be interpreted as exploratory comparisons among plots.

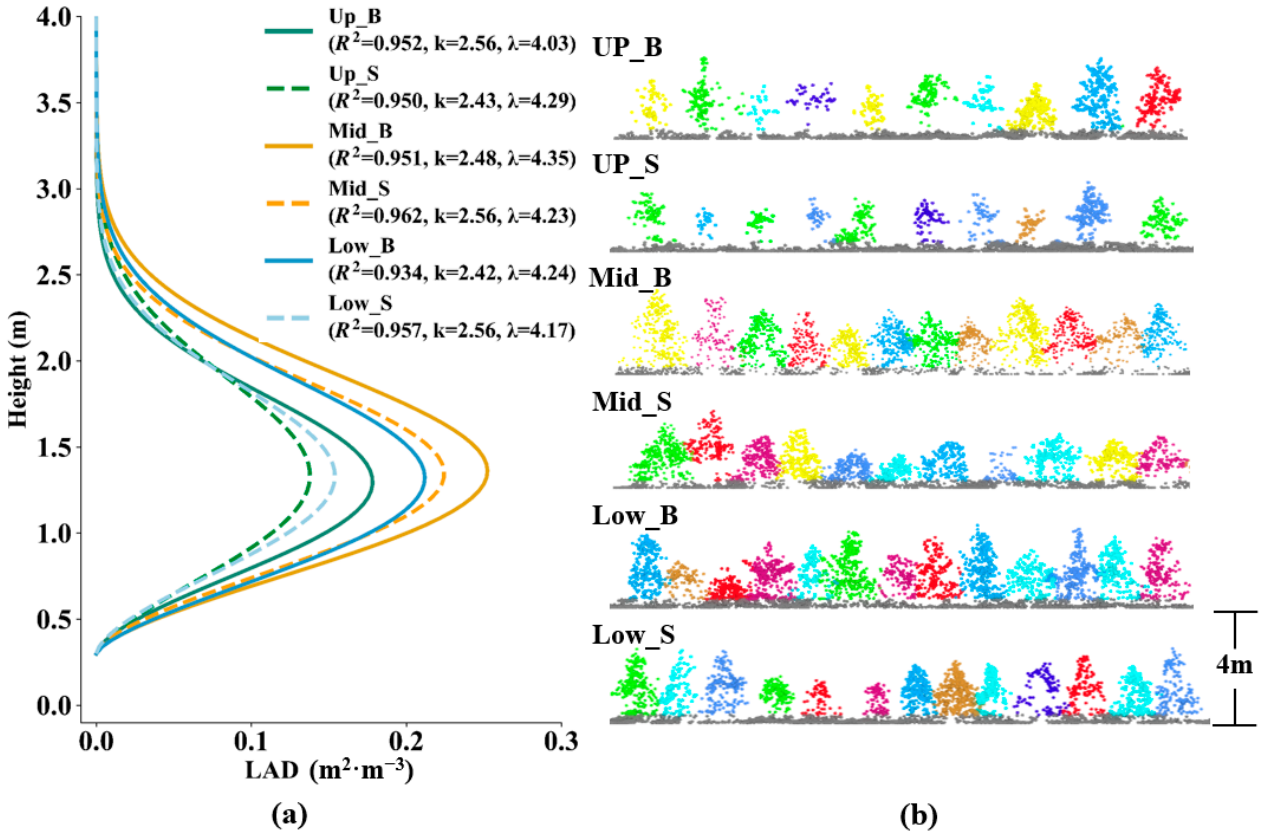


Figure 11. Vertical LAD profiles and point cloud distributions for plots differing in slope position and planting pit size. (**a**) Vertical LAD profiles fitted using the Weibull function, with R^2 and the estimated parameters shown for each plot; (**b**) corresponding point-cloud profiles of representative belt transects, with colors indicating segmented individual trees.

4. Discussion

4.1. Reliability of UAV-LiDAR for Monitoring Growth in Young Chinese Fir Plantations

Accurate measurement of early tree growth is essential for evaluating plantation establishment and management practices. UAV-LiDAR achieved consistently high individual-tree detection accuracy across all plots, with F-scores exceeding 0.95, likely because of the open canopy and limited crown overlap. These results agree with previous UAV-LiDAR studies in young pine and Chinese fir plantations [22,24]. Nevertheless, the mean F-score declined slightly from 0.981 to 0.966 with increasing planting density (Figure 5b), consistent with evidence that greater stand density and crown overlap complicate individual-tree segmentation [43–45]. Manual correction involved approximately 2–5 trees per 20 × 20 m plot, indicating that the workflow was operationally feasible for young, open-canopy plantations, although its scalability may be limited in larger or structurally more complex stands.

Because DGL could not be directly retrieved from the top-down UAV-LiDAR observations, the TH–DGL model extended the bi-temporal analysis from LiDAR-derived TH change to model-based DGL change. The model was calibrated using November measurements and applied consistently to both survey dates. For the eight trees with TH values of 0.5–1.5 m in the independent November validation dataset, the relative errors of TH, DGL, and AGB were comparable to or lower than those for the complete validation dataset, supporting model performance for smaller trees within the available data. However, these November trees may have differed in growth status and height–diameter allocation from younger February trees of similar height. Because field measurements were available only in November, the temporal stability of the TH–DGL relationship and the February

estimates could not be independently evaluated. Applying the same model to both dates maintained methodological consistency, while possible developmental changes in height–diameter allocation remain a source of uncertainty in ΔDGL.

Uncertainty in AGB and ΔAGB arose from the sequential use of LiDAR-derived TH, model-estimated DGL, and the allometric equation. At the individual-tree scale, TH was retrieved with an RMSE of 0.29 m, part of which may reflect uncertainty in field-measured height [46,47]. Errors introduced through the TH–DGL model may subsequently propagate into AGB estimates [48], and diameter errors can contribute more strongly to biomass uncertainty than height errors [49]. The selected allometric equation was developed for three-year-old Chinese fir in Fujian Province and uses DGL and TH as predictors, making it a reasonable choice for young trees that had not all reached breast height. However, its applicability to trees at different developmental stages remains uncertain. Applying the same equation to both dates provided a consistent basis for temporal comparison, although developmental differences in biomass allocation may affect the absolute AGB and ΔAGB estimates. Plot-level aggregation reduced relative errors by averaging some individual-tree errors but could not remove systematic uncertainty associated with the models. Overall, bi-temporal UAV-LiDAR provided reliable individual-tree detection and TH-change estimates, while the TH–DGL model and allometric equation extended the workflow to DGL and AGB growth assessment.

4.2. Scale-Dependent Growth Responses to Establishment Practices

Planting density affected radial and area-based growth more clearly than height growth in young Chinese fir. TH varied little among density treatments, whereas DGL and individual tree AGB were significantly greater under low density than under medium and high density. Density-related differences were therefore more evident in radial development and individual-tree biomass than in tree height, consistent with previous studies showing that diameter growth in young Chinese fir is more sensitive to stand density than height growth [50,51]. At the plot scale, however, ΔAGB was significantly higher under high density than under low density because the greater number of trees per unit area compensated for lower individual-tree biomass accumulation. Whether this early pattern persists will depend on how canopy closure and competition develop with stand age [51,52]. The contrasting density-related patterns in single-date individual-tree attributes and model-derived plot-level biomass increments highlight the value of UAV-LiDAR in characterizing stand performance at different scales. Bi-temporal UAV-LiDAR provides information on tree attributes and biomass accumulation at both individual-tree and plot scales. With longer time series, it could be used to track density-related growth, tree-size differentiation, and increasing competition as stands develop [53].

Growth and biomass accumulation also varied among the six slope-position and planting-pit-size plots. Because each combination was represented by only one plot, these patterns are interpreted as descriptive, plot-specific variation. Growth generally increased toward the lower slope, whereas differences between large- and small-pit plots were greatest at the upper slope, particularly for AGB and ΔAGB. The upper-slope pattern is consistent with the hypothesis that larger planting pits provide greater initial rooting space and alleviate local establishment constraints [54]. However, soil water and nutrient availability were not measured, and their roles could not be evaluated directly. These observations therefore support further replicated experiments rather than a general conclusion about planting-pit effects across topographic positions [55].

4.3. Associations Between Canopy Structural Variation and Biomass Accumulation

Canopy structure determines the three-dimensional distribution of foliage and thereby affects light interception and biomass production [56,57]. Individual-tree crown dimensions and relative positions describe growing space and competition, whereas plot-level CC, LAI, and LAD profiles characterize collective canopy occupation. Previous studies have shown that UAV-LiDAR-derived crown metrics can provide information on competition not fully captured by stem diameter or tree position [58]. The strong Weibull fits to the LAD profiles presented in Figures 9 and 11 ($R^2 > 0.93$ for all fitted profiles shown) supported the use of k and λ to summarize vertical foliage organization [21,59], complementing conventional tree-size estimates.

Planting density altered the balance between individual-tree growth and plot-level biomass accumulation (Figure 8). Low density favored individual-tree development, whereas high density promoted area-based biomass accumulation. Although only LAD_{max} differed significantly among treatments (Table 6; Figure 9), ΔAGB was strongly associated with LAI and CC, positively associated with LAD_{max} and foliage peak height, and negatively associated with Weibull *k*. The negative correlation with *k* suggests that greater biomass accumulation coincided with a broader vertical foliage distribution. Overall, biomass accumulation was more closely linked to foliage quantity and canopy closure than to LAD profile shape, reflecting the density trade-off between individual-tree growth and collective canopy occupation [58]. As canopy closure proceeds, structural metrics may become more sensitive to the cumulative effects of management.

Across the six slope-position and planting-pit-size plots, canopy structural metrics and biomass showed different spatial patterns (Table 7; Figure 11). In the large-pit plots, LAI, CC, and LAD_{max} were highest at the middle slope, whereas biomass generally increased toward the lower slope. This mismatch suggests that canopy organization represents an important, but not exclusive, pathway linking establishment conditions to biomass accumulation. Because each combination was represented by one plot, these patterns remain descriptive. Nevertheless, integrating tree-level growth and plot-level canopy metrics can strengthen UAV-LiDAR assessments of competition and density regulation [60]. LAD estimates based on a fixed extinction coefficient are more suitable for relative comparisons than absolute quantification [61–63]. The relatively open canopies of young Chinese fir facilitated LiDAR penetration and the characterization of vertical foliage distribution. However, in denser stands, further optimizing flight altitude, flight-line configuration, and overlap, as well as using sensors with smaller beam divergence, higher pulse energy, and reliable multiple-return recording, may improve lower-canopy sampling [64].

5. Conclusions

This study used bi-temporal UAV-LiDAR to estimate growing-season increments at the individual-tree and plot scales and to characterize differences in three-dimensional canopy structure under different plantation establishment conditions in young Chinese fir plantations. Consistent tree correspondence across surveys enabled TH changes to be derived directly from bi-temporal UAV-LiDAR observations, while a TH–DGL model and an allometric equation were used to estimate changes in DGL and AGB.

Low planting density was associated with larger individual-tree DGL and AGB, whereas high density had greater plot-level ΔAGB than low density. Although only LAD_{max} differed significantly among density treatments, ΔAGB was positively related to LAI, CC, LAD_{max}, and foliage peak height and negatively related to Weibull *k*. Together, these findings show that bi-temporal UAV-LiDAR can characterize density responses across individual-tree and plot scales while revealing canopy–biomass associations not captured by tree-size metrics alone.

Exploratory comparisons across slope-position and planting-pit-size plots revealed additional plot-specific variation in growth and canopy structure. Tree size, area-based biomass accumulation, and three-dimensional canopy organization represent related but distinct dimensions of early plantation development. Integrating bi-temporal growth estimates with three-dimensional canopy metrics provides a cross-scale approach for monitoring young, open-canopy plantations. However, because field measurements were available only in November 2023, the accuracy of the bi-temporal growth increments could not be independently validated, and ΔDGL and ΔAGB retained uncertainty associated with the TH–DGL model and allometric equation. Given the single-site design and unreplicated slope-position × planting-pit-size combinations, the applicability of these findings to other species, sites, and closed-canopy stands requires further evaluation.

Author Contributions: Conceptualization, project administration, H.Z.; data curation, investigation, X.L. and B.Y.; formal analysis, validation, visualization, writing—original draft preparation, X.L.; funding acquisition, H.Z. and J.M.C.; methodology, H.Z. and Z.H.; supervision, H.Z., J.M.C. and Z.H.; writing—review and editing, X.L., H.Z. and B.Y. All authors have read and agreed to the published version of the manuscript.

Funding: This research was funded by the National Natural Science Foundation of China, grant number 42471128; the Fujian Provincial Key Forestry Science and Technology Research Program, grant number 2026FKJ1; and the Education Department Project of Fujian Province, grant number K20230069.

Data Availability Statement: The data presented in this study are available on request from the corresponding author.

Acknowledgments: The authors are grateful to Sirong Wang of Baisha Forest Farm, Shanghang, for assistance with plot management and maintenance, and to undergraduate students Ruoy Zhang, Jiazhi Mo, and Yaxin Lin for their help with the field survey.

Conflicts of Interest: The authors declare no conflicts of interest.

References

1. Pan, Y.; Birdsey, R.A.; Fang, J.; Houghton, R.; Kauppi, P.E.; Kurz, W.A.; Phillips, O.L.; Shvidenko, A.; Lewis, S.L.; Canadell, J.G.; et al. A Large and Persistent Carbon Sink in the World's Forests. *Science* **2011**, *333*, 988–993. https://doi.org/10.1126/science.1201609.
2. Baskent, E.Z. A Framework for Characterizing and Regulating Ecosystem Services in a Management Planning Context. *Forests* **2020**, *11*, 102. https://doi.org/10.3390/f11010102.
3. Lamb, D.; Erskine, P.D.; Parrotta, J.A. Restoration of Degraded Tropical Forest Landscapes. *Science* **2005**, *310*, 1628–1632. https://doi.org/10.1126/science.1111773.
4. Shangguan, Y.; Zhao, H.; Zhang, Z.; Xu, E.; Lv, D.; Wang, Y.; Zhao, X.; Wei, N.; Chen, G.; Liu, J.; et al. Carbon Storage and Sequestration of Five Planting Patterns of *Picea crassifolia* Plantations in Qilian Mountains. *Front. Earth Sci.* **2025**, *13*, 1560899. https://doi.org/10.3389/feart.2025.1560899.
5. Benomar, L.; Lamhamedi, M.S.; Rainville, A.; Beaulieu, J.; Bousquet, J.; Margolis, H.A. Genetic Adaptation vs. Ecophysiological Plasticity of Photosynthetic-Related Traits in Young *Picea glauca* Trees along a Regional Climatic Gradient. *Front. Plant Sci.* **2016**, *7*, 48. https://doi.org/10.3389/fpls.2016.00048.
6. Duan, J.; Ma, L.Y.; Jia, L.M.; Xu, C.Y.; Jia, Z.K.; Che, W.R. The Density Effect of *Platycladus orientalis* Plantation in Beijing Area. *AES* **2010**, *30*, 3206–3214. https://doi.org/10.20103/j.stxb.2010.12.014.
7. Forrester, D.I. Linking Forest Growth with Stand Structure: Tree Size Inequality, Tree Growth or Resource Partitioning and the Asymmetry of Competition. *For. Ecol. Manage.* **2019**, *447*, 139–157. https://doi.org/10.1016/j.foreco.2019.05.053.
8. Korbik, M.; Swoczyna, T.; Latocha, P. Pre-Planting and Planting Factors and Practices Affecting Urban Tree Growth: With a Special Focus on the Root System and Its Condition—A Review. *Plants* **2025**, *14*, 387. https://doi.org/10.3390/plants14030387.

9. Tyagi, V.; Singh, S.P.; Singh, R.D.; Gumber, S.; Thadani, R.; Pandey, R. Influence of Slope Position and Aspect on the Vegetation Attributes and Tree-Water Relations in Forests of the Central Himalayas. *J. Mt. Sci.* **2023**, *20*, 2592–2602. https://doi.org/10.1007/s11629-023-7967-z.
10. Liao, J.; Zhang, X.; Rademacher, T.; Xu, C.; Du, M.; Guo, F.; Li, W.; Zheng, J.; Wu, Y.; Manzanedo, R.D. Slope Mediates Drought Sensitivity but Does Not Affect Drought Recovery for Young Trees along Elevation Gradients in Temperate Planted Larch Forests. *For. Ecosyst.* **2025**, *14*, 100371. https://doi.org/10.1016/j.fecs.2025.100371.
11. Tian, Q.; Tian, F. Weakening Mountain Vegetation Aspect Asymmetry Due to Altered Energy Conditions. *Nat. Clim. Change* **2026**, *16*, 193–199. https://doi.org/10.1038/s41558-025-02542-4.
12. Dănescu, A.; Albrecht, A.T.; Bauhus, J. Structural Diversity Promotes Productivity of Mixed, Uneven-Aged Forests in Southwestern Germany. *Oecologia* **2016**, *182*, 319–333. https://doi.org/10.1007/s00442-016-3623-4.
13. Fotis, A.T.; Murphy, S.J.; Ricart, R.D.; Krishnadas, M.; Whitacre, J.; Wenzel, J.W.; Queenborough, S.A.; Comita, L.S. Above-ground Biomass Is Driven by Mass-ratio Effects and Stand Structural Attributes in a Temperate Deciduous Forest. *J. Ecol.* **2018**, *106*, 561–570. https://doi.org/10.1111/1365-2745.12847.
14. Kunwar, S.; Wang, L.-Q.; Chaudhary, R.; Joshi, P.R.; Ali, A. Stand Density of Co-Existing Species Regulates above-Ground Biomass along a Local-Scale Elevational Gradient in Tropical Forests. *Appl. Veg. Sci.* **2021**, *24*, e12577. https://doi.org/10.1111/avsc.12577.
15. Zellweger, F.; De Frenne, P.; Lenoir, J.; Vangansbeke, P.; Verheyen, K.; Bernhardt-Römermann, M.; Baeten, L.; Hédl, R.; Berki, I.; Brunet, J.; et al. Forest Microclimate Dynamics Drive Plant Responses to Warming. *Science* **2020**, *368*, 772–775. https://doi.org/10.1126/science.aba6880.
16. De Frenne, P.; Lenoir, J.; Luoto, M.; Scheffers, B.R.; Zellweger, F.; Aalto, J.; Ashcroft, M.B.; Christiansen, D.M.; Decocq, G.; De Pauw, K.; et al. Forest Microclimates and Climate Change: Importance, Drivers and Future Research Agenda. *Glob. Change Biol.* **2021**, *27*, 2279–2297. https://doi.org/10.1111/gcb.15569.
17. Wu, X.; Niu, C.; Liu, X.; Hu, T.; Feng, Y.; Zhao, Y.; Liu, S.; Liu, Z.; Dai, G.; Zhang, Y.; et al. Canopy Structure Regulates Autumn Phenology by Mediating the Microclimate in Temperate Forests. *Nat. Clim. Change* **2024**, *14*, 1299–1305. https://doi.org/10.1038/s41558-024-02164-2.
18. Hardiman, B.S.; Bohrer, G.; Gough, C.M.; Vogel, C.S.; Curtis, P.S. The Role of Canopy Structural Complexity in Wood Net Primary Production of a Maturing Northern Deciduous Forest. *Ecology* **2011**, *92*, 1818–1827. https://doi.org/10.1890/10-2192.1.
19. Ehbrecht, M.; Schall, P.; Juchheim, J.; Ammer, C.; Seidel, D. Effective Number of Layers: A New Measure for Quantifying Three-Dimensional Stand Structure Based on Sampling with Terrestrial LiDAR. *For. Ecol. Manage* **2016**, *380*, 212–223. https://doi.org/10.1016/j.foreco.2016.09.003.
20. Coops, N.C.; Hilker, T.; Wulder, M.A.; St-Onge, B.; Newnham, G.; Siggins, A.; Trofymow, J.A. Estimating Canopy Structure of Douglas-Fir Forest Stands from Discrete-Return LiDAR. *Trees* **2007**, *21*, 295–310. https://doi.org/10.1007/s00468-006-0119-6.
21. Zhang, Z.; Cao, L.; She, G. Estimating Forest Structural Parameters Using Canopy Metrics Derived from Airborne LiDAR Data in Subtropical Forests. *Remote Sens.* **2017**, *9*, 940. https://doi.org/10.3390/rs9090940.
22. Rodríguez-Puerta, F.; Gómez-García, E.; Martín-García, S.; Pérez-Rodríguez, F.; Prada, E. UAV-Based LiDAR Scanning for Individual Tree Detection and Height Measurement in Young Forest Permanent Trials. *Remote Sens.* **2021**, *14*, 170. https://doi.org/10.3390/rs14010170.
23. Cosenza, D.N.; Vogel, J.; Broadbent, E.N.; Silva, C.A. Silvicultural Experiment Assessment Using Lidar Data Collected from an Unmanned Aerial Vehicle. *For. Ecol. Manage.* **2022**, *522*, 120489. https://doi.org/10.1016/j.foreco.2022.120489.
24. Zhou, X.; Ma, K.; Sun, H.; Li, C.; Wang, Y. Estimation of Forest Stand Volume in Coniferous Plantation from Individual Tree Segmentation Aspect Using UAV-LiDAR. *Remote Sens.* **2024**, *16*, 2736. https://doi.org/10.3390/rs16152736.
25. Fu, X.; Zhang, Z.; Cao, L.; Coops, N.C.; Goodbody, T.R.H.; Liu, H.; Shen, X.; Wu, X. Assessment of Approaches for Monitoring Forest Structure Dynamics Using Bi-Temporal Digital Aerial Photogrammetry Point Clouds. *Remote Sens. Environ.* **2021**, *255*, 112300. https://doi.org/10.1016/j.rse.2021.112300.
26. Riofrío, J.; White, J.C.; Tompalski, P.; Coops, N.C.; Wulder, M.A. Harmonizing Multi-Temporal Airborne Laser Scanning Point Clouds to Derive Periodic Annual Height Increments in Temperate Mixedwood Forests. *Can. J. For. Res.* **2022**, *52*, 1334–1352. https://doi.org/10.1139/cjfr-2022-0055.
27. Qi, Z.; Li, S.; Pang, Y.; Zheng, G.; Kong, D.; Li, Z. Assessing Spatiotemporal Variations of Forest Carbon Density Using Bi-Temporal Discrete Aerial Laser Scanning Data in Chinese Boreal Forests. *For. Ecosyst.* **2023**, *10*, 100135. https://doi.org/10.1016/j.fecs.2023.100135.

28. Xiong, J.; Zeng, H.; Cai, G.; Li, Y.; Chen, J.M.; Miao, G. Crown Information Extraction and Annual Growth Estimation of a Chinese Fir Plantation Based on Unmanned Aerial Vehicle–Light Detection and Ranging. *Remote Sens.* **2023**, *15*, 3869. https://doi.org/10.3390/rs15153869.
29. Yin, D.; Wang, L.; Lu, Y.; Shi, C. Mangrove Tree Height Growth Monitoring from Multi-Temporal UAV-LiDAR. *Remote Sens. Environ.* **2024**, *303*, 114002. https://doi.org/10.1016/j.rse.2024.114002.
30. Coops, N.C.; Tompalski, P.; Goodbody, T.R.H.; Queinnec, M.; Luther, J.E.; Bolton, D.K.; White, J.C.; Wulder, M.A.; Van Lier, O.R.; Hermosilla, T. Modelling Lidar-Derived Estimates of Forest Attributes over Space and Time: A Review of Approaches and Future Trends. *Remote Sens. Environ.* **2021**, *260*, 112477. https://doi.org/10.1016/j.rse.2021.112477.
31. Yu, Z.; Qi, J.; Zhao, X.; Huang, H. Evaluating the Reliability of Bi-Temporal Canopy Height Model Generated from Airborne Laser Scanning for Monitoring Forest Growth in Boreal Forest Region. *Int. J. Digital Earth* **2024**, *17*, 2345725. https://doi.org/10.1080/17538947.2024.2345725.
32. Chen, Q.; Baldocchi, D.; Gong, P.; Kelly, M. Isolating Individual Trees in a Savanna Woodland Using Small Footprint Lidar Data. *Photogramm. Eng. Remote Sens.* **2006**, *72*, 923–932. https://doi.org/10.14358/PERS.72.8.923.
33. Lin, G.; Fan, S.; He, Z.; Yang, X.; Ying, J.; Lu, S. A Study on the Influence of Site Management Measures on the Growth of 3-year-old Cunninghamia lanceolata Plantation of Second-generation. *For. Res.* **2001**, *14*, 403–407. https://doi.org/10.13275/j.cnki.lykxyj.2001.04.009.
34. Liu, D.; Fan, W.; Li, M. Estimation of Forest Stand Parameters and Biomass by Small-Footprint Lidar. *J. Northeast. For. Univ.* **2012**, *40*, 39–43. https://doi.org/10.13759/j.cnki.dlxb.2012.01.025.
35. Preece, N.D.; Lawes, M.J.; Rossman, A.K.; Curran, T.J.; van Oosterzee, P. Modelling the Growth of Young Rainforest Trees for Biomass Estimates and Carbon Sequestration Accounting. *For. Ecol. Manage.* **2015**, *351*, 57–66. https://doi.org/10.1016/j.foreco.2015.05.003.
36. Annighöfer, P.; Mund, M.; Seidel, D.; Ammer, C.; Ameztegui, A.; Balandier, P.; Bebre, I.; Coll, L.; Collet, C.; Hamm, T.; et al. Examination of Aboveground Attributes to Predict Belowground Biomass of Young Trees. *For. Ecol. Manage.* **2022**, *505*, 119942. https://doi.org/10.1016/j.foreco.2021.119942.
37. Virtanen, P.; Gommers, R.; Oliphant, T.E.; Haberland, M.; Reddy, T.; Cournapeau, D.; Burovski, E.; Peterson, P.; Weckesser, W.; Bright, J.; et al. SciPy 1.0: Fundamental Algorithms for Scientific Computing in Python. *Nat. Methods* **2020**, *17*, 261–272. https://doi.org/10.1038/s41592-019-0686-2.
38. Xu, K.; Zeng, H.; Chang, C.; Xie, J.; Yang, Y. Relating Forest Phenology to Temperature and Precipitation in the Subtropical Region of Fujian Based on Time-Series MODIS-NDVI. *J. Geo-Inf. Sci.* **2015**, *17*, 1249–1259. Available online: https://www.dqxxkx.cn/CN/abstract/article/1560-8999/36993.
39. Wan, D.; Yang, Z.; Liu, X.; Xiong, D.; Xu, C.; Chen, S.; Yang, Y. Subtropical tree saplings growth phenology based on solid-state Lidar altimetry and its response to environmental factors. *Chin. J. Plant Ecol.* **2025**, *49*, 2080–2091. https://doi.org/10.17521/cjpe.2024.0138.
40. Li, W.; Guo, Q.; Jakubowski, M.K.; Kelly, M. A New Method for Segmenting Individual Trees from the Lidar Point Cloud. *Photogramm. Eng. Remote Sens.* **2012**, *78*, 75–84. https://doi.org/10.14358/PERS.78.1.75.
41. Liu, K.; Shen, X.; Cao, L.; Wang, G.; Cao, F. Estimating Forest Structural Attributes Using UAV-LiDAR Data in Ginkgo Plantations. *ISPRS J. Photogramm. Remote Sens.* **2018**, *146*, 465–482. https://doi.org/10.1016/j.isprsjprs.2018.11.001.
42. Goutte, C.; Gaussier, E. A Probabilistic Interpretation of Precision, Recall and F-Score, with Implication for Evaluation. In *Advances in Information Retrieval*; Losada, D.E., Fernández-Luna, J.M., Eds.; Lecture Notes in Computer Science; Springer Berlin Heidelberg: Berlin, Heidelberg, 2005; Volume 3408, pp. 345–359. ISBN 978-3-540-25295-5.
43. Falkowski, M.J.; Smith, A.M.S.; Gessler, P.E.; Hudak, A.T.; Vierling, L.A.; Evans, J.S. The Influence of Conifer Forest Canopy Cover on the Accuracy of Two Individual Tree Measurement Algorithms Using Lidar Data. *Can. J. Remote Sens.* **2008**, *34*, S338–S350. https://doi.org/10.5589/m08-055.
44. Vauhkonen, J.; Ene, L.; Gupta, S.; Heinzel, J.; Holmgren, J.; Pitkanen, J.; Solberg, S.; Wang, Y.; Weinacker, H.; Hauglin, K.M.; et al. Comparative Testing of Single-Tree Detection Algorithms under Different Types of Forest. *Forestry* **2012**, *85*, 27–40. https://doi.org/10.1093/forestry/cpr051.
45. Hamraz, H.; Contreras, M.A.; Zhang, J. Forest Understory Trees Can Be Segmented Accurately within Sufficiently Dense Airborne Laser Scanning Point Clouds. *Sci. Rep.* **2017**, *7*, 6770. https://doi.org/10.1038/s41598-017-07200-0.
46. Andersen, H.-E.; Reutebuch, S.E.; McGaughey, R.J. A Rigorous Assessment of Tree Height Measurements Obtained Using Airborne Lidar and Conventional Field Methods. *Can. J. Remote Sens.* **2006**, *32*, 355–366. https://doi.org/10.5589/m06-030.

47. Ganz, S.; Käber, Y.; Adler, P. Measuring Tree Height with Remote Sensing—A Comparison of Photogrammetric and LiDAR Data with Different Field Measurements. *Forests* **2019**, *10*, 694. https://doi.org/10.3390/f10080694.
48. Fang, R. Impacts of Tree Height-Dbh Allometry on Lidar-Based Tree Aboveground Biomass Modeling. *Int. Arch. Photogramm. Remote Sens. Spat. Inf. Sci.* **2016**, *XLI-B8*, 625–628. https://doi.org/10.5194/isprs-archives-XLI-B8-625-2016.
49. Tupinambá-Simões, F.; Pascual, A.; Guerra-Hernández, J.; Ordóñez, C.; Barreiro, S.; Bravo, F. Combining Hand-Held and Drone-Based Lidar for Forest Carbon Monitoring: Insights from a Mediterranean Mixed Forest in Central Portugal. *Eur. J. For. Res.* **2025**, *144*, 925–940. https://doi.org/10.1007/s10342-025-01772-7.
50. Tong, S.; Sheng, W.; Zhang, J. Studies on the Density Effects of Chinese Fir Stands. *For. Res.* **2002**, *15*, 66–75. https://doi.org/10.13275/j.cnki.lykxyj.2002.01.011.
51. Pretzsch, H. Density and Growth of Forest Stands Revisited. Effect of the Temporal Scale of Observation, Site Quality, and Thinning. *For. Ecol. Manage.* **2020**, *460*, 117879. https://doi.org/10.1016/j.foreco.2020.117879.
52. Long, S.; Zeng, S.; Wang, G. Dynamics of Stand Density and Self-Thinning in Chinese Fir Plantations: Theoretical Insights and Empirical Validation. *Front. Plant Sci.* **2024**, *15*, 1444807. https://doi.org/10.3389/fpls.2024.1444807.
53. Gavilan-Acuna, G.; Coops, N.C.; Tompalski, P.; Roeser, D.; Varhola, A. The Use and Integration of Airborne Laser Scanning and Satellite Time Series Data in Precision Forest Management for Plantations of Fast-Growing Tree Species. *Ann. For. Sci.* **2025**, *82*, 22. https://doi.org/10.1186/s13595-025-01292-9.
54. Mauki, D.; Kilonzo, M. Planting Pit Size Determines Successful Tree Seedling Establishment in Arid and Semi-Arid Region of Tanzania. *Environ. Sustain. Indic.* **2022**, *15*, 100197. https://doi.org/10.1016/j.indic.2022.100197.
55. Löf, M.; Dey, D.C.; Navarro, R.M.; Jacobs, D.F. Mechanical Site Preparation for Forest Restoration. *N. For.* **2012**, *43*, 825–848. https://doi.org/10.1007/s11056-012-9332-x.
56. Binkley, D.; Campoe, O.C.; Gspaltl, M.; Forrester, D.I. Light Absorption and Use Efficiency in Forests: Why Patterns Differ for Trees and Stands. *For. Ecol. Manage.* **2013**, *288*, 5–13. https://doi.org/10.1016/j.foreco.2011.11.002.
57. Ehbrecht, M.; Seidel, D.; Annighöfer, P.; Kreft, H.; Köhler, M.; Zemp, D.C.; Puettmann, K.; Nilus, R.; Babweteera, F.; Willim, K.; et al. Global Patterns and Climatic Controls of Forest Structural Complexity. *Nat. Commun.* **2021**, *12*, 519. https://doi.org/10.1038/s41467-020-20767-z.
58. Puletti, N.; Guasti, M.; Innocenti, S.; Cesaretti, L.; Chiavetta, U. A Semi-Automatic Approach for Tree Crown Competition Indices Assessment from UAV LiDAR. *Remote Sens.* **2024**, *16*, 2576. https://doi.org/10.3390/rs16142576.
59. Liu, H.; Zhang, Z.; Cao, L. Estimating Forest Stand Characteristics in a Coastal Plain Forest Plantation Based on Vertical Structure Profile Parameters Derived from ALS Data. *Natl. Remote Sens. Bull.* **2018**, *22*, 872–888. https://doi.org/10.11834/jrs.20187465.
60. Chen, C.; Zhou, L.; Li, X.; Zhao, Y.; Yu, J.; Lv, L.; Du, H. Optimizing the Spatial Structure of *Metasequoia* Plantation Forest Based on UAV-LiDAR and Backpack-LiDAR. *Remote Sens.* **2023**, *15*, 4090. https://doi.org/10.3390/rs15164090.
61. Wang, W.-M.; Li, Z.-L.; Su, H.-B. Comparison of Leaf Angle Distribution Functions: Effects on Extinction Coefficient and Fraction of Sunlit Foliage. *Agric. For. Meteorol.* **2007**, *143*, 106–122. https://doi.org/10.1016/j.agrformet.2006.12.003.
62. Richardson, J.J.; Moskal, L.M.; Kim, S.-H. Modeling Approaches to Estimate Effective Leaf Area Index from Aerial Discrete-Return LIDAR. *Agric. For. Meteorol.* **2009**, *149*, 1152–1160. https://doi.org/10.1016/j.agrformet.2009.02.007.
63. Awaya, Y.; Araki, K. Estimating Three-Dimensional Distribution of Leaf Area Using Airborne LiDAR in Deciduous Broad-Leaved Forest. *Remote Sens.* **2023**, *15*, 3043. https://doi.org/10.3390/rs15123043.
64. Zeng, H.D.; Li, Y.F.; Chen, J.M.; Miao, G.F.; Wang, R.; Xiong, J.F. Estimating Forest Leaf Area Index Using Discrete Point Clouds from UAV-LiDAR Systems with Different Canopy Penetration Capacities. *Remote Sens. Environ.* **2026**, *344*, 115512. https://doi.org/10.1016/j.rse.2026.115512.

Disclaimer/Publisher's Note: The statements, opinions and data contained in all publications are solely those of the individual author(s) and contributor(s) and not of MDPI and/or the editor(s). MDPI and/or the editor(s) disclaim responsibility for any injury to people or property resulting from any ideas, methods, instructions or products referred to in the content.